

# High-Resolution Radar Imaging of Mercury's North Pole

J. K. Harmon and P. J. Perillat

*National Astronomy and Ionosphere Center, Arecibo Observatory, HC3 Box 53995, Arecibo, Puerto Rico 00612*

E-mail: [harmon@naic.edu](mailto:harmon@naic.edu)

and

M. A. Slade

*Jet Propulsion Laboratory, California Institute of Technology, MS 238-420, 4800 Oak Grove Drive, Pasadena, California 91109*

Received May 10, 2000; revised September 12, 2000

The recently upgraded Arecibo S-band ( $\lambda 12.6$ -cm) radar was used to make delay-Doppler images of Mercury's north polar region, where earlier observations had shown strong echoes from putative ice deposits in craters. The image resolution of 1.5–3 km is a substantial improvement over the 15-km resolution of the older Arecibo images (J. K. Harmon *et al.* 1994, *Nature* 369, 213–215). The new observations confirm all the original polar features and reveal many additional features, including several at latitudes as low as 72–75°N and several from craters less than 10 km in diameter. All of the new features located on the Mariner-imaged side of the planet can be matched with known craters or other shaded areas. We find the north pole to be located 65 km from the original Mariner-based pole and 15 km from the new Mariner-based pole of M. S. Robinson *et al.* (1999, *J. Geophys. Res.* 104, 30,847–30,852). The improved resolution reveals fine structure in the radar features and their respective host craters, including radar shadowing/highlighting by central peaks and rim walls, rim terracing, and preferential concentration of radar-bright deposits in shaded southern floor areas. The radar features' high brightness, circular polarization inversion ( $\mu_c = 1.25$ ), and confinement to regions permanently shaded from direct sunlight are all consistent with volume scattering from a cold-trapped volatile such as clean water ice. The sizes and locations of most of the features show good agreement with the thermal model of A. R. Vasavada, D. A. Paige, and S. E. Wood (1999, *Icarus* 141, 179–193) for insulated (buried) water ice, although the problems of explaining radar features in small craters and the rapid burial required at lower latitudes suggest that other factors may be suppressing ice loss after emplacement. © 2001 Academic Press

**Key Words:** Mercury; Radar; Ices.

## 1. INTRODUCTION

Radar imaging of Mercury in 1991–1992 at Goldstone/VLA (Very Large Array) and at Arecibo revealed strong, highly depolarized echoes coming from the planet's north and south poles (Slade *et al.* 1992, Harmon and Slade 1992, Butler *et al.* 1993).

The polar locations of these bright features, and their resemblance to echoes from the three icy Galilean satellites and Mars' south polar cap, immediately suggested that polar ice might exist on Mercury. The idea that permanently shaded areas at Mercury's poles could harbor ice deposits had, in fact, been entertained years earlier (Thomas 1974, Kumar 1976), as had a similar idea for polar ice on the Moon (Watson *et al.* 1961, Arnold 1979). Preliminary thermal modeling (Paige *et al.* 1992, Ingersoll *et al.* 1992, Salvail and Fanale 1994), and the identification of a south polar feature in Chao Meng-Fu Crater (Harmon and Slade 1992), supported the notion that polar craters on Mercury might be cold traps for water ice. Additional support came from improved polar images derived from reanalysis and averaging of the 1991–1992 Arecibo data. These images, which had a resolution of 15 km, resolved both the north and south polar features into numerous crater-size spots, many of which coincided with the positions of known craters on the Mariner-10 images (Harmon *et al.* 1994).

The Arecibo telescope recently underwent a major upgrading. One of the objectives of the upgrade was to gain an order-of-magnitude improvement in the sensitivity of the S-band radar through a combination of a doubling of the transmitter power and replacement of the line feed with a more efficient Gregorian subreflector system. When the upgrade was successfully completed in the spring of 1998, one of our first priorities was to use the new radar to do better imaging of Mercury's poles. Our goals were to search for smaller and/or weaker features and to resolve details in some of the known features. We were particularly interested in seeing if improved imaging would reveal any bright features at latitudes lower than that of the lowest (79°) features seen in 1991–1992. Another important consideration was the fact that Mercury's sub-Earth longitude at the time of maximum polar visibility had precessed by about 180° since the 1991–1992 observations, which meant that whole new regions of the pole could be observed from a more favorable aspect.

With these objectives in mind, we undertook a series of Mercury radar observations in mid-August of 1998, when the planet’s north pole was near its optimum visibility. These, the first delay-Doppler observations with the new radar, yielded high-quality polar images with 3-km resolution, representing a significant advance over the previous work. Follow-up observations in July, 1999 yielded additional images of the north pole with resolutions down to 1.5 km. (Unfortunately, equipment failure prevented us from making south polar observations that had been planned for March, 1999.) In this paper we present the new north polar images and discuss their implications for the polar ice hypothesis.

## 2. OBSERVATIONS AND DATA ANALYSIS

### 2.1. Observing Epochs

The observations were made with the S-band (2380 MHz;  $\lambda = 12.6$  cm) radar on the 305-m Arecibo telescope. The images presented in this paper were derived from observations made on pairs of consecutive dates at three different epochs: August 16 and 17, 1998; July 2 and 3, 1999; July 25 and 26, 1999. The August 16/17 and July 25/26 observations were made just after inferior conjunction at planet distances of 0.63 and 0.59 AU, respectively. The July 2/3 observations were made at a less favorable range of 0.76 AU. The mean sub-Earth points for the various dates were: 174.1°W, 11.27°N (August 16); 180.9°W, 11.07°N (August 17); 352.7°W, 7.32°N (July 2); 357.8°W, 7.55°N (July 3); 135.0°W, 11.75°N (July 25); 141.7°W, 11.73°N (July 26).

### 2.2. Transmission/Reception

The transmitted power ( $P$ ), antenna gain ( $G$ ), and system temperature ( $T$ ) were 900 KW, 72.0 dB, and 27 K, respectively. For comparison, the corresponding parameters for the old (pre-upgrade) radar system were 420 KW, 70.8 dB, and 32 K. This represented a factor of 4.5 improvement in effective radar system sensitivity  $PG^2/T$  or, taking the square, a factor of 20 reduction in the integration time required to achieve the same signal-to-noise ratio, all other factors being equal.

A circularly polarized wave was transmitted. The transmission was bi-phase coded using either a 1023-length pseudorandom code with a 20- $\mu$ s baud (for August 16/17 and July 2/3) or a 2047-length code with 10- $\mu$ s baud (for July 25/26). Both combinations gave a 20.46-ms code cycle which was longer than Mercury’s 16.3-ms delay depth, thus avoiding any delay folding of the echo. The corresponding frequency bandwidth of 48.9 Hz ( $=1/20.46$  ms) was smaller than the planet’s Doppler bandwidth, which resulted in some echo aliasing. It is worth noting here that the pre-upgrade Arecibo imaging (Harmon and Slade 1992, Harmon *et al.* 1994) was done using an unconventional long-code technique, which employs a non-repeating code to avoid the aliasing associated with echo overspreading. Since a long-code capability was not yet available on the new system, and given that our primary interest was in imaging the pole rather than the full Mercury disk, we elected to proceed with

the 1998–1999 observations using conventional repeating-code pulse compression.

The received signal was quadrature mixed to base band, passed through either 20- $\mu$ s or 10- $\mu$ s matched filters, complex sampled once per baud, and recorded for off-line analysis. Both the orthogonal-circular (“OC” or “polarized”) and same-circular (“SC” or “depolarized”) polarization senses were received and recorded. Following standard practice, the observations were organized into “runs,” each consisting of a transmit period one round-trip light travel time in duration followed by a receive period of the same duration.

### 2.3. Delay-Doppler Analysis

We applied the standard intercode delay-Doppler analysis appropriate for a repeating-code waveform. After decoding, the coherent (Doppler) analysis was done using either 1024- or 2048-length Fourier transforms, which gave frequency resolutions of 0.0477 Hz (August 25/26 and July 2/3) or 0.0239 Hz (July 25/26). About 30 realizations (or “looks”) of the  $1023 \times 1024$  (or  $2047 \times 2048$ ) delay-Doppler array were summed incoherently to give an average delay-Doppler array for each polarization (OC, SC) for each run. From each of these run-averaged arrays we subtracted a noise baseline level estimated from the power in the echo-free delay bins. The array values were then normalized to units of radar cross section, using the measured system parameters and noise baseline level to calibrate. The calibration was checked by comparing the total SC cross sections with values from continuous-wave (CW) observations made at the same sub-Earth longitudes using the old (pre-upgrade) system. This comparison showed excellent agreement.

The aforementioned Doppler aliasing produced some visible folding of the leading-edge echo, but this had a negligible effect at the polar delays. Another artifact from use of a repeating code was echo leakage into the code’s delay sidelobes. Although the effect on the SC echo was negligible, we had to make corrections for leakage of the strong specular echo in the OC polarization in order to obtain reliable polarization ratios for the polar features (see Section 5.2).

### 2.4. Mapping and Accuracy

The final analysis step was a mapping from delay-Doppler coordinates to planetary (latitude–longitude) coordinates. This mapping used ephemeris-derived values for the planet’s Doppler bandwidth, true-to-apparent spin axis angle, and sub-Earth point coordinates, and assumed an equatorial radius of 2439.0 km and an obliquity of zero. A separate mapping was done for each run’s average delay-Doppler array. The run-averaged maps were then summed to make a final map for each two-day epoch. A total of 10, 6, and 11 runs were averaged to make the August 25/26, July 2/3, and July 25/26 images, respectively. The map resolution cell dimensions were set by the baud length in the delay (line-of-sight) direction and by the frequency resolution in the transverse direction. This corresponded to a  $3.0 \times 2.2$ -km

resolution cell for the the August 16/17 and July 2/3 images, and a  $1.5 \times 1.1$ -km resolution cell for the July 25/26 image.

The positional (coordinate gridding) accuracy of the images was determined mainly by our precision in estimating the delay-Doppler position of the sub-Earth point at the reference altitude, which was itself determined by our accuracy in removing any residual delay and Doppler offsets introduced through errors in the real-time data-taking ephemeris. To estimate these offsets we computed topographic profiles from the leading edge of the OC echo using the technique described in Harmon *et al.* (1986). The profiles from the various runs were rotated about their sub-Earth points to remove relative Doppler errors between runs on a given day, and then tied to the sub-Earth point of the adjacent day to remove the absolute Doppler error. The final profiles were then compared with profiles in Harmon *et al.* (1986) to remove any remaining systematic error in absolute altitude relative to the 2439.0-km datum. After making all these corrections we estimate the final positional accuracy of the images (relative to the planet coordinate grid) to be about 2 km ( $0.05^\circ$ ) in both the delay and Doppler directions.

The familiar north-south ambiguity problem that plagues most delay-Doppler mapping was not a problem for our polar imaging as most of the the south polar region (and any associated “ice” features) was well hidden behind the radar horizon. The few remaining spots that could conceivably have come from low-latitude south polar features were all confirmed as northern features based on the consistency of their mapped positions between different epochs or different days of the same epoch. (The mapped location of a south polar feature incorrectly assumed to come from the north will shift with time as Mercury’s sub-Earth latitude and apparent spin axis change.)

### 3. POLAR FEATURES: LOCATIONS AND HOST CRATERS

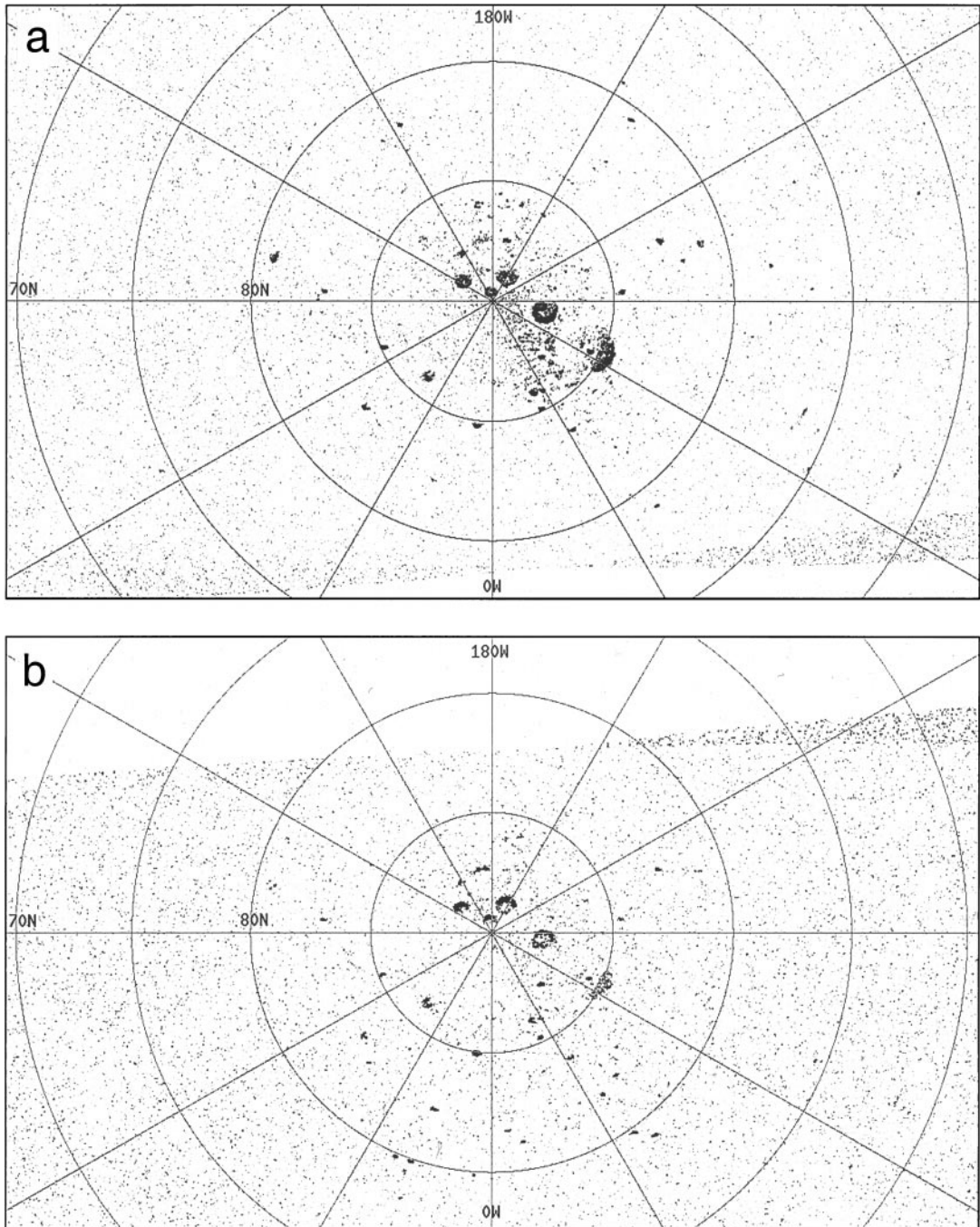
In Figs. 1a, 1b, and 2a we show polar-projection images of the depolarized (SC) echo for the three epochs. (We do not show OC images in this paper as they are very similar to the SC images but have a lower signal-to-noise ratio owing to a slightly higher system temperature in the OC channel, some clutter contribution from code sidelobe leakage of the OC specular echo, and the fact that the polar “ice” features are intrinsically weaker in the OC polarization.) Figures 1a and 1b show the 20- $\mu$ s images from August 16/17 and July 2/3, respectively, and Fig. 2a shows the 10- $\mu$ s image from July 25/26. Note that the radar illumination direction differs by  $180^\circ$  of longitude between Figs. 1a and 1b, which shows up in the reversed crater floor visibilities and rim highlights. Note also that the July 2/3 image is noisier than the other two images, a consequence of the larger planet distance and higher incidence angles at that epoch.

Figure 2b maps the locations of radar features seen in Figs. 1a, 1b, and 2a. All of these features (except X2) exceeded 5.5 noise standard deviations for at least one of the three epochs; the image coverage in Figs. 1 and 2 was chosen so as to encompass all polar bright features with peak brightness exceeding this noise thresh-

old. Figure 3a shows a smaller-scale image derived by summing the images from the August 16/17 and July 25/26 epochs. Overplotted circles show the locations of the rims of the features’ host craters based on our own adjusted version of the new Mariner-derived map of Robinson *et al.* (1999); this adjusted map grid is discussed in detail in Section 3.3. Figure 3b shows the corresponding positions of these same host craters on the original Mariner-based NASA/USGS maps (Davies *et al.* 1978, Grolier and Boyce 1984). The day side at the time of the Mariner-10 encounters corresponds to the hemisphere to the left of the  $10$ – $190^\circ$ W meridian; following Harmon *et al.* (1994), we will refer to this as the “photographed” side. Terrain to the right of the  $10$ – $190^\circ$ W meridian corresponds to the “unphotographed hemisphere,” which remains terra incognita to spacecraft imaging. Figures 2b and 3 use the same labels for features A–Y as in Harmon *et al.* (1994); this labeling system was itself an extension of the A–G crater labels adopted by Paige *et al.* (1992). For new features we continue with letter Z, followed by A2, B2, ..., Z2, A3, B3, etc. We have assigned letter labels to any new features mentioned specifically in the text, which includes most of the new features on the photographed side and several features of interest on the unphotographed side. In our discussion of certain features we will also refer to specific crater classifications from the north polar geologic map of Grolier and Boyce (1984), both to point out the types of craters containing radar features and to aid the reader in locating those craters on that map. Specifically, we will refer to some craters as being of  $c_4$  class (the youngest and least degraded) or  $c_3$  class (older and more degraded).

#### 3.1. “Old” (Previously Seen) Features

All of the north polar features seen in the old (1991–1992) Arecibo images (Harmon *et al.* 1994) can also be seen in some or all of the new images. As before, the most conspicuous features are D, E, H, J, and K. All five of these features now show definite crater structure, as will be discussed in detail in Sections 4.1 and 4.2. Features D and E had previously been identified with two known  $c_4$ -class craters based on the old image, although E appeared to be in contact with another feature (H) which was presumed to come from a separate crater on the unphotographed side just beyond the Mariner-10 terminator. The new images now resolve E and H into separate features. As in the old image, feature C shows up as a relatively faint feature occupying the southern floor of another  $c_4$ -class crater, while the brighter feature Y comes from a smaller crater on the east rim of crater C. The lower-latitude features L, M, N, P, R, and W can be seen in each of the three images (Figs. 1a, 1b, and 2a), whereas Q, S, and T show up in one or both of the 1999 images (Figs. 1b and/or 2a) but are invisible in the 1998 image (Fig. 1a) owing to a lack of radar-visible floor at such high incidence angles. Features M, N, R, S, and W are all identified with  $c_4$ -class craters. Both M and W are of particular interest here, being well-resolved features whose positions can now be accurately located in the floors of their relatively large host craters (see Section 4.3). Feature W, which lies in crater Despréz, was the only one of the original



**FIG. 1.** Twenty-microsecond north polar SC images from Arecibo radar observations on (a) August 16/17, 1998, and (b) July 2/3, 1999. Darker shades correspond to higher echo strength. The radar illumination is from the top in (a) (mean sub-Earth longitude =  $177.5^\circ\text{W}$ ) and from the bottom in (b) (mean sub-Earth longitude =  $356.8^\circ\text{W}$ ). The blank areas at the bottom of (a) and the top of (b) correspond to regions beyond the radar horizon.

north polar features to be identified with a named crater. Features S and T were noteworthy as having the lowest latitudes of any features on the photographed side of the 1991–1992 images (Harmon *et al.* 1994). All of the smaller unlabeled features on the unphotographed side of the 1991–1992 image, including several strung out roughly along the  $320^\circ\text{W}$  meridian, show up in some or all of the new images. The faint “diffuse patch” that was seen

near the pole (Harmon *et al.* 1994) can also be discerned in the new images.

### 3.2. “New” Features

As expected, no new large features were found in the 1998–1999 images. However, we were able to identify many new small

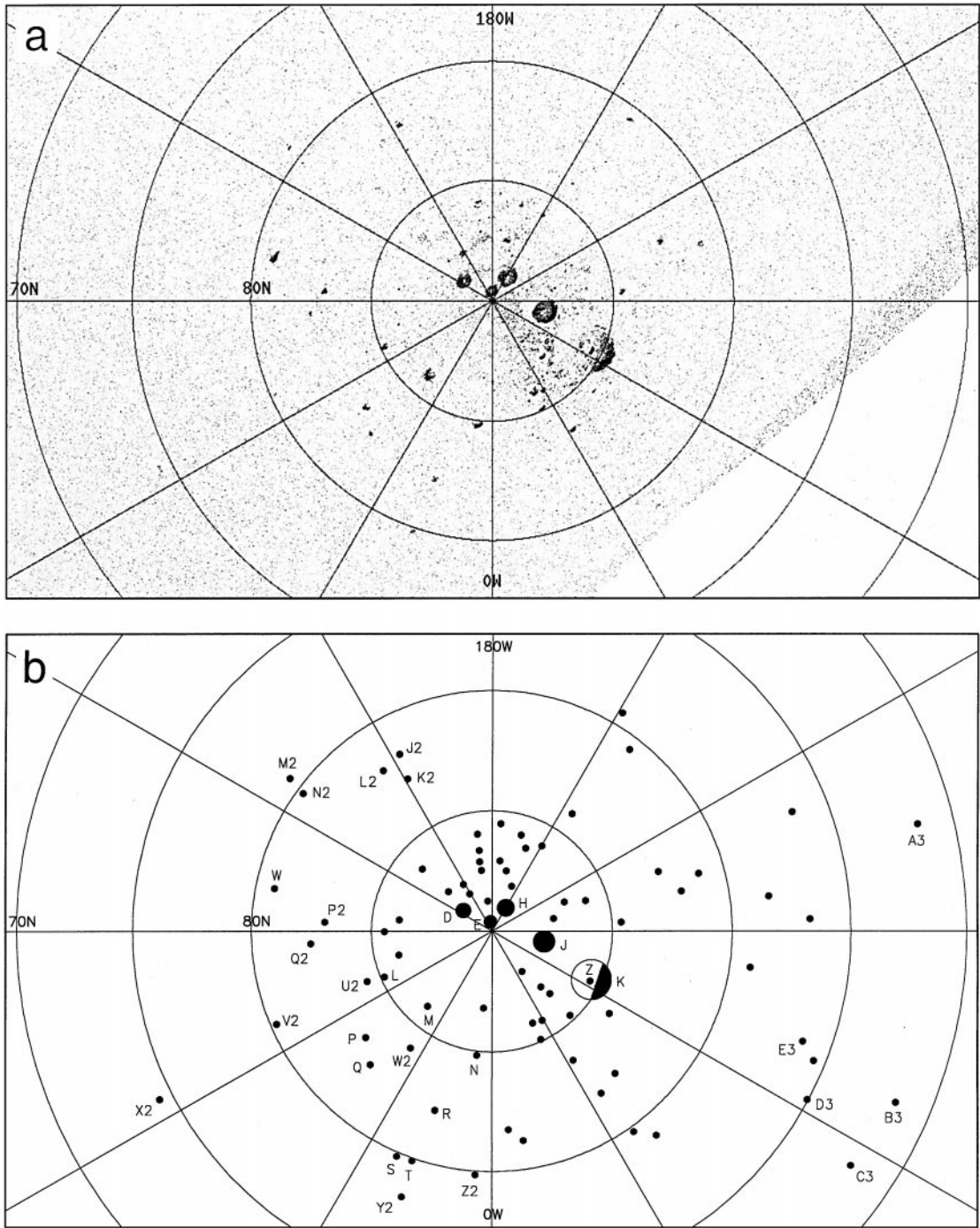


**FIG. 2.** (a) Ten-microsecond north polar SC image from Arecibo radar observations on July 25/26, 1999. The radar illumination is from the upper left (mean sub-Earth longitude =  $138.0^{\circ}\text{W}$ ), and the region beyond the radar horizon is at the lower right. (b) Map showing the locations of radar-bright features seen in Figs. 1a, 1b, and 2a.

features thanks to a combination of improved resolution, higher signal-to-noise ratio, and different sub-Earth aspect.

**3.2.1. Photographed side.** The upper half of Fig. 3a reveals many new features that now show up with the more favorable radar illumination from the  $180^{\circ}\text{W}$  side. A fairly dense cluster

of these is located north of  $85^{\circ}\text{N}$  and just south of features D, E, and H. Two of these, B and F, correspond to two medium-size craters in the original Paige *et al.* (1992) list of likely host craters. Crater A, a rather large and irregular  $c_3$ -class crater, shows only faint features in its east and south floors and a small feature in its north floor that probably comes from an interior crater. Like

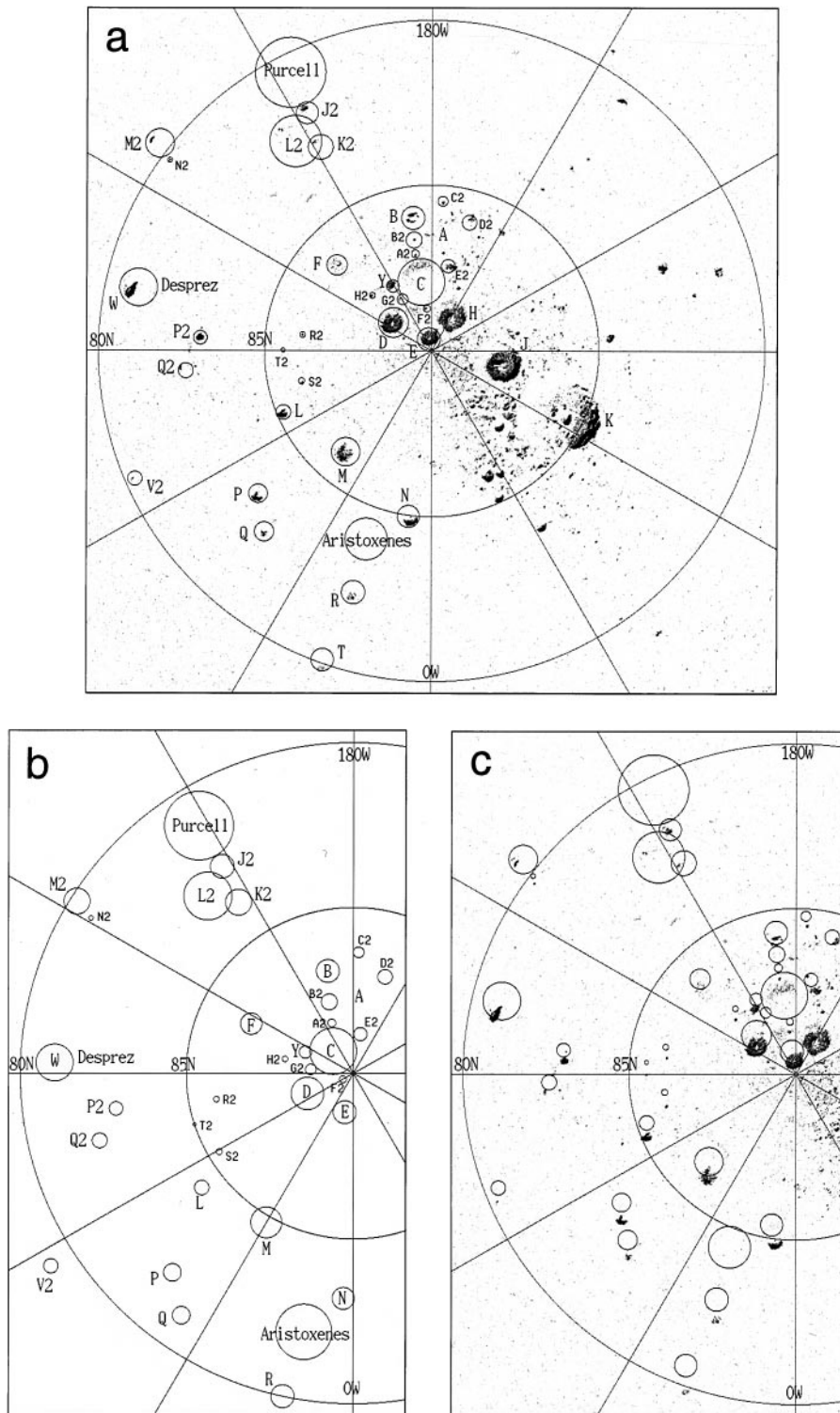


**FIG. 3.** (a) Radar image formed by summing the SC images from August 16/17, 1998, and July 25/26, 1999. The locations of host-crater rims (lettered circles) are based on a shift-and-stretch adjustment to the locations in the revised Mariner-based grid of Robinson *et al.* (1999). Also shown for reference are the locations of the  $c_3$ -class craters Purcell and Aristoxenes. The irregular rim of crater A is circumscribed by craters A2, B2, B, C2, D2, E2, and C. (b) Locations of feature host craters in the original Mariner-based maps (Davies *et al.* 1978, Grolier and Boyce 1984). (c) Same as (a), but using the Robinson *et al.* (1999) crater positions without adjustment.

B, several other features (A2, B2, C2, D2, E2) can be traced to smaller craters clustered around the rim of crater A. One of these craters (A2) is less than 10 km in size. Other features traced to small (<10 km) craters in this region include F2 (on the north rim of crater C) and H2 (east of crater Y).

Several other new features were found in the upper left portion of Fig. 3a. A  $c_4$ -class crater on the north rim of Purcell contains a moderately bright feature (J2), while weaker features are seen in a  $c_4$ -class crater (K2) just to its north and in the south floor of a  $c_3$ -class crater (L2) to its northeast. No features can be seen in Purcell itself, a large  $c_3$ -class crater. Between Purcell and Despréz we find a feature (M2) in a medium-size  $c_4$ -class crater at 79.5°N. A small (<10 km) crater on the north rim of crater M2 is identified as the source of feature N2.

Several new features were found in the extension of the Borealis smooth plains north of Crater Despréz (W) and Goethe basin. The most prominent of these is feature P2, located midway between W and L. Just southeast of P2 is another feature (Q2) from a similar-sized crater in the rim of Goethe basin. A scarp running between these two craters also shows a bright feature on its shaded side. Further north, just northwest of crater L, are three very small features (R2, S2, T2), each of which can be traced to a crater less than 10 km in diameter. Feature U2 (southwest of crater L) does not coincide with any obvious crater, though it does come from a shaded spot in the Mariner-10 images. Two other small, faint features can be traced to craters in the interior of Goethe basin; these are V2 (in western Goethe) and W2 (located in a <10-km crater on the northeast edge of the basin floor). Just south of Goethe we found another faint feature (X2) located in the southern floor of crater Tung Yuan, a prominent (65 km diameter)  $c_4$ -class crater. Although this feature does not exceed 5.5 standard deviations in any given image, it shows up in all three epochs and is clearly a real feature. At 74.5°N, this feature has the lowest latitude of any feature on the photographed side and, hence, the lowest latitude of any feature for which we have a host-crater identification.

Two new low-latitude features have been found near the bottom of the July 2/3 image (see Figs. 1b and 2b). Feature Y2 has been traced to a crater located two degrees south of Crater T. The other (Z2) is located in a crater on the Mariner-10 terminator east of Crater T.

**3.2.2. Unphotographed side.** The majority of the low-latitude features are found on the dark side of the Mariner-10 terminator (see the right-hand sides of Figs. 1 and 2). Here 13 features were found at latitudes below 80°N, with the 3 lowest (A3, B3, C3) located between 71.6°N and 71.9°N. All 13 are statistically significant (>5.5 s.d.) in at least one epoch, and although most show up clearly in only one epoch, this probably reflects nothing more than the strong aspect dependence of radar shadowing at high incidence angles near the radar horizon. Furthermore, 10 of these features are clearly visible in both days of the 1998 epoch, and one of the features below 72°N (B3) is visible in both the 1998 (Fig. 1a) and July 2/3, 1999 (Fig. 1b) images. All of the low-latitude features are small, which would

be consistent with the very limited amount of permanent shading expected at these latitudes. Even the most extended features (B3, E3) are both shaped like slivers with their long sides facing the pole, suggesting that they are located in very narrow regions of permanent shading under the south rims of their respective host craters (similar to feature M2 on the photographed side). The concentration of these low-latitude features (and feature X2) within about 30° of the 90–270°W longitude meridian, and the corresponding lack of features at such low latitudes along the 0–180°W meridian, indicates some preference of the volatiles for “cold longitudes” (270°W and 90°W) over “hot longitudes” (0°W and 180°W). Here, the “hot longitudes” refer to the alternating subsolar longitudes at Mercury perihelion; the equatorial points at these longitudes are sometimes referred to as the “hot poles.”

A number of other new features can be seen nearer the pole on the unphotographed side. Among them are some distinct features that can be resolved out of the diffuse patch west of craters J and K.

### 3.3. Polar Grid and Pole Location

There are sizable systematic differences between feature positions on the radar grid (Fig. 3a) and positions of their respective host craters on the original NASA/USGS grid (Fig. 3b). This was first pointed out by Harmon *et al.* (1994), who ascribed the discrepancy to systematic error in the inherently less accurate NASA/USGS grid. As a first-order correction, Harmon *et al.* suggested sliding the NASA/USGS grid down by 1.6° (68 km) along the prime meridian, although they also noted a scale distortion that required an even larger correction for the area around craters R, S, and T at the bottom of the Borealis region map (Grolier and Boyce 1984).

Recent work has been done on constructing an improved mapping control net for Mercury based on a reanalysis of Mariner-10 data (Davies *et al.* 1996, Robinson *et al.* 1999). This has given revised positions for the north and south poles as well as scale-distortion corrections. The result is a new Mariner-based map grid (Robinson *et al.* 1999) which is in much better agreement with the radar-derived grids shown in Harmon *et al.* (1994) and this paper. Figure 3c shows the revised locations of polar craters from Robinson *et al.* (1999) overplotted on the new Arecibo image from Fig. 3a. Note that there remains some residual discrepancy between the crater locations and radar features. Since the radar accuracy is about an order of magnitude better than the 25-km accuracy of the revised Mariner-based positions in Robinson *et al.* (1999), we conclude that most of this discrepancy is error in the revised Mariner-based grid. We found we could remove nearly all of this discrepancy by shifting Robinson's crater locations down along the 0° meridian by 0.35° (15 km), followed by a 2% pole-centered stretch along this same axis and a small (0.035°) right shift. Here we have relied on the smaller features to do the registration in order to minimize bias from radar features being off-center in their host-crater floors. The result is the set of crater positions shown as

overlaid circles in Fig. 3a. These crater positions relocate the north pole to a position close to that specified by Harmon *et al.* (1994) and approximately 65 km from the original NASA/USGS location.

#### 4. POLAR FEATURES: DETAILED STRUCTURE

The higher resolution of the new images has enabled us to better resolve individual features as well as determine their precise locations in the floors of their host craters. The structural details discussed here are best seen in Fig. 4, which shows central portions of Figs. 1a and 2a. We also refer to Fig. 3a when discussing the locations of the features within their host craters.

##### 4.1. Features D, E, H, and J, and the “Diffuse Patch”

The radar features from the medium-size craters D, E, H, and J are well resolved and show interior structure. All four features show structure from central peaks; these peaks cast radar shadows and also show some highlighting on their radar-facing slopes. The brightest echoes from these craters are associated with slope-induced highlighting of the radar-facing portions of their lower interior rim walls (see Section 5.1). Also, all four of these features have a slightly ovoid or lens-shaped appearance, an effect of radar shadowing by the near rim. The aspect-dependent nature of these wall highlighting and radar shadowing effects are easily seen by comparing Figs. 4a and 4b (where the radar direction changes by  $40^\circ$ ). The overall impression from the size, circularity, and structure of features D, E, H, and J is that most of their crater floor areas, including the lower rim wall slopes, are covered with radar-bright material. This can also be seen from the extent of features D and E relative to their crater rims (Fig. 3a).

Surrounding the bright crater features are radar-dark halos which we interpret to be ice-free terrain on the high, exposed crater rims. These dark halos stand out only because they contrast with the “diffuse patch,” the modestly enhanced and largely unresolved brightness that can be seen concentrated mainly above  $85^\circ\text{N}$  on the unphotographed side. The diffuse patch may arise from ice deposits in a dense collection of small shaded areas in the ejecta blankets of these craters (see Section 6.1.5). Some of the diffuse patch is also associated with shading by the rims of these craters; the best example of this is the tongue of diffuse brightness that goes up the shaded area between craters D and E and spreads out below the north rim of crater C.

##### 4.2. Feature K

This feature was the largest and most irregular of the bright north polar features in the old (1991–1992) image. It is now clear that feature K comes from the southern floor area of a large crater roughly 90 km in diameter. This crater, which is comparable in size to the northern craters Purcell and Jokai (see the map of Grolier and Boyce (1984)), is the second largest “icy” crater that we have found on Mercury; only the south polar crater Chao Meng-Fu (155 km diameter) is larger. The

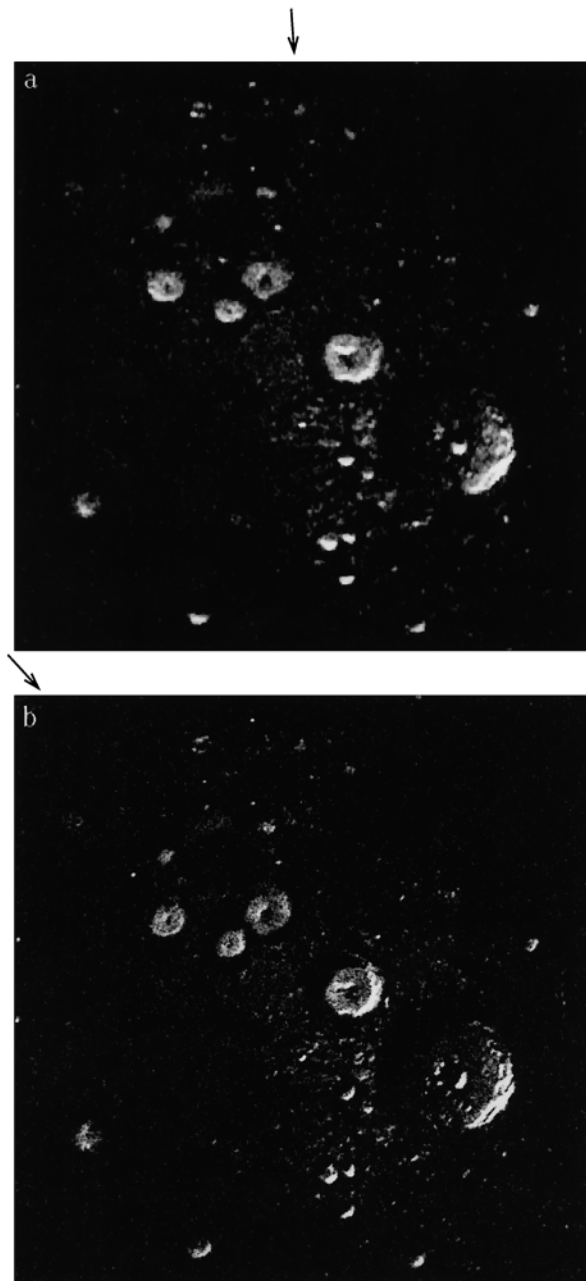


**FIG. 4.** Detail of central portions of the radar images from (a) August 16/17, 1998, and (b) July 25/26, 1999. Lighter shades correspond to higher echo strength. The radar illumination directions are indicated (arrows). Surface resolution is 3 km in (a) and 1.5 km in (b).

main bright area in K coincides with that portion of crater floor which should be perpetually shaded by the south rim. For a cylindrical, flat-floored crater, the permanently shaded part is the segment of a circle contained between the southern (equatorward) rim and an east–west chord whose center distance  $x$  from the south rim is given by  $x \approx d \tan \phi$ , where  $d$  is the crater depth and  $\phi$  is the latitude of the south rim. For crater K we estimate  $x$  to be 34 km, or about 38% of the crater diameter,

which is in good agreement with the shape of the observed feature. The fact that the Chao Meng-Fu feature is much more circular than feature K can be attributed to its closer proximity to the pole and correspondingly more complete floor coverage by volatiles.

Like the other prominent features, feature K shows some highlighting from the radar-facing portion of the southern interior rim. This highlighting clearly shows some terrace structure. The northern half of the (otherwise radar-dark) floor shows several bright spots. The most prominent of these (Z), located near the crater center, is the brightest single feature in our north polar images. The shape of this feature and its change with radar aspect (Fig. 4) are consistent with near-wall radar shadowing, indicating that this feature comes from a central crater rather than a central peak. That our clearest example of a radar feature in a nested crater should also be our brightest feature may not be coincidence. This may be an example of the double-shielding effect of Carruba and Coradini (1999), which predicts very low temperatures for craters embedded in the floors of older, larger craters owing to the extra shielding from indirect radiation. Crater Z may actually experience only partial double-shielding, being located just outside the bright floor segment in K, although the effect may still be enough to significantly lower the average temperature inside the crater.

North of the radar-dark part of the floor of crater K is an even darker area similar to the dark haloes around craters D, E, H, and J. Again, we would interpret this as ice-free terrain of the exposed north rim of crater K along with some radar shadow. To the northwest and west of this is some diffuse brightness mixed with brighter discrete features. The clustering of these features in this region suggests that at least some of them may be secondary craters from the K (or J) impacts.

#### 4.3. Other Features

We have been able to resolve many other features besides those just discussed. One of the larger of these, feature M, has a distinctive crescent shape with cusps facing toward the pole (Figs. 3a and 4). Figure 3a shows that this radar feature is offset slightly toward the southern portion of its host crater. Figure 3a also shows that feature W is concentrated in the southern floor of crater Despréz. The fact that feature W occupies a smaller fraction of its crater floor than does feature M is consistent with its lower latitude. Feature M2 also follows this trend, being 1.5° lower in latitude than W and showing only a small sliver of radar feature under its south rim (Fig. 3a). Inspection of Fig. 3a shows several other features (C, P, N, R, T, Y, J2, K2, L2, Q2) concentrated in the southern floors of their host craters. Features L and P appear as pole-oriented crescents similar to feature M. Other small features showing some resolved structure include the various features just west of crater K. Most of these features show crescent or segment shapes with orientations that change depending on the direction of radar illumination (compare Figs. 4a and 4b), an indication of rim-wall radar shadowing and highlighting.

## 5. POLAR FEATURES: RADAR SCATTERING PROPERTIES

Some quantitative discussion of the basic radar scattering parameters of the polar features is required in order to draw comparisons with other observations and to gain some insight into the scattering process. Here we consider two basic radar properties of the features, brightness and polarization.

### 5.1. Radar Cross Sections and Albedos

Table I lists the total SC radar cross sections  $\sigma_{sc}$  (in km<sup>2</sup>) measured for the prominent features D, E, H, J, and K. These were obtained from the August 1998 image, when each feature was observed at the tabulated mean incidence angle  $\theta$ . Such raw cross sections will be useful for making direct comparisons with images obtained at other telescopes and/or wavelengths. In addition, to give a meaningful measure of feature brightness that compensates for incidence angle, we estimate an equivalent full-disk SC albedo  $\hat{\sigma}_{sc} = 2\sigma_{sc}^0(\theta)/(n+1)\cos^n\theta$ . Here  $\hat{\sigma}_{sc}$  is the SC albedo (total radar cross section  $\sigma_{sc}$  divided by planet projected area  $\pi r^2$ ) that the entire planet would have if it conformed to a  $\sigma_{sc}^0(\theta) \propto \cos^n\theta$  scattering law, where  $\sigma_{sc}^0(\theta)$  is the specific cross section measured for a given scattering element at incidence angle  $\theta$ . Echoes from the icy Galilean satellites are well approximated by limb-darkened ( $n > 1$ ) cosine laws, with  $n = 1.5$  for Ganymede and Callisto and  $n = 1.8$  for Europa (Ostro *et al.* 1992). A value of  $n = 1.77$  was estimated for Mars' south polar cap echo based on Goldstone measurements between incidence angles of 65° and 77° (Harmon *et al.* 1999). Since our Mercury data span an insufficient range of incidence angles to estimate  $n$  reliably, we will simply assume an  $n = 1.5$  scattering law based on these earlier results. From this we derived the equivalent full-disk SC albedos  $\hat{\sigma}_{sc}$  listed in Table I. These are averages over the “flat-floor” portion of each feature, which excludes highlights and shadows from rim slopes and central peaks. We get an area-averaged  $\hat{\sigma}_{sc}$  of 0.89 for these features. For comparison, the full-disk depolarized albedos of the icy Galilean satellites are in the range 0.4–1.6 (Ostro *et al.* 1992) and the equivalent full-disk albedo of Mars' southern ice cap is 0.5–0.6 at X-band ( $\lambda 3.5$  cm) (Butler 1994, Harmon *et al.* 1992, Harmon *et al.* 1999). From this it is clear that Mercury's polar features are comparable in

**TABLE I**  
**Radar Scattering Parameters**

Feature	$\theta$ (°)	$\sigma_{sc}$ (km <sup>2</sup> )	$\hat{\sigma}_{sc}$	$\mu_c$
D	78.0	57	0.79	1.31
E	78.5	35	0.96	1.21
H	77.8	63	0.66	1.19
J	79.3	152	0.90	1.23
K	81.1	188	0.99	1.28
Avg.			0.89	1.25

*Note.* Estimated calibration errors are 15–20% for  $\sigma_{sc}$  and  $\hat{\sigma}_{sc}$  and less than 5% for  $\mu_c$ . An error of 0.2 in the assumed cosine power law exponent  $n$  would add an additional error of  $\approx 25\%$  to  $\hat{\sigma}_{sc}$ .

brightness to the anomalously bright backscatter from Galilean satellite and martian ice.

The bright highlighting of the radar-facing inner walls of some of these larger craters is apparently an incidence-angle effect from the interior rim slopes rather than an intrinsic brightness difference. The rim highlight from feature J, for example, is 3.4 times brighter than the floor. To get this highlight from a slope effect alone (assuming an  $n = 1.5$  cosine law) requires the rim to have a slope of  $14^\circ$ , which agrees with typical rim-wall slopes for mercurian craters of this size (Pike 1988). An even shallower slope ( $11^\circ$ ) is sufficient to explain the rim highlight if one uses the  $n = 1.77$  value obtained for Mars' south polar cap over a similar incidence angle range. Our presumption in all this, of course, is that these lower wall slopes are "icy" and backscatter by the same mechanism as the floors. Arecibo radar observations of the Moon by Stacy *et al.* (1997) revealed some bright, highly depolarized (i.e., "ice-like") spots in the unshaded, radar-facing interior walls of some lunar craters and basins, which they attributed to conventional scattering from extreme wavelength-scale roughness. While it is possible that the rimwall highlights we see from craters such as J and K contain some contribution from this effect, their rather uniform appearance and restriction to the polar region suggests that the "icy slope" effect is dominant. Note also that the unshaded northern wall of crater K shows no sign of any feature, let alone a highlight, even when favorably illuminated as in Fig. 1b. Finally, the fact that features such as X2 (Tung Yuan) and B3 do not change position with illumination direction suggests that such low-latitude features cannot be explained away as rough-surface scattering from rim walls.

### 5.2. Circular Polarization Ratios

Another diagnostic scattering parameter that we measure is the circular polarization ratio  $\mu_c = \sigma_{sc}/\sigma_{oc}$ . For specular reflection there is no depolarization ( $\mu_c = 0$ ), whereas diffuse reflection from wavelength-scale roughness can show significant depolarization (but with the ratio normally satisfying  $\mu_c < 1$ ). Enhanced backscatter from extraterrestrial ices, which is apparently a volume scattering effect, is associated with systematic circular polarization inversion ( $\mu_c > 1$ ). The icy Galilean satellites (Europa, Ganymede, Callisto), which are the prototypes for anomalous ice backscatter (Campbell *et al.* 1978), all show this inversion. These bodies have disk-averaged  $\mu_c$  values in the range 1.15–1.5 at both S and X bands, and this inversion is maintained out to very high incidence angles near the limbs (Ostro *et al.* 1992). The enhanced backscatter from the south polar ice cap of Mars also shows an inverted polarization ratio (Muhleman *et al.* 1991).

In order to make reliable  $\mu_c$  estimates for our polar features, we first had to correct the OC delay-Doppler array for the effects of leakage of the strong specular echo into delay sidelobes of the code. This leakage produced visible streaking at the polar delays (except near zero Doppler) and complicated the noise baseline estimation. As a first-order leakage correction we performed a crude deconvolution as follows: an initial

flat noise baseline was estimated and subtracted from the raw delay-Doppler array; next, we convolved each frequency of this array with the calculated code sidelobes for that frequency to estimate a delay-Doppler leakage array; the leakage array was least-squares adjusted to the level of the raw delay-Doppler array using the echo-free delays, and then subtracted from the raw delay-Doppler array, removing both the leakage streaks and the true flat noise baseline in the process. Although this algorithm was effective in removing the visible leakage streaks, its main effect on our  $\mu_c$  estimates came from correcting the noise baseline subtraction. This was demonstrated by the fact that the  $\mu_c$  estimates in Table I are very close to those obtained by simply using the echo-free region near zero-Doppler to estimate a baseline level without doing a full leakage subtraction.

In Table I we list  $\mu_c$  values estimated for the major features by dividing the SC cross sections by OC cross sections from the leakage-corrected OC images. Each value represents an average over the entire feature, including highlights. The area-averaged  $\mu_c$  for all of these features is 1.25, which is in good agreement with the inverted ratios measured from the 1991–1992 Arecibo data (Harmon *et al.* 1994). The north polar  $\mu_c$  values measured from the X-band Goldstone/VLA images were in the range 1.0–1.4 (Slade *et al.* 1992). Clearly, the polarization inversion of Mercury's north polar features is well established from a variety of observations.

## 6. IMPLICATIONS FOR POLAR ICE

The case for the existence of polar ice on Mercury rests on evidence that the radar features (1) have radar scattering characteristics similar to those of the icy Galilean satellites and Mars' southern ice cap and (2) are located in permanently shaded floors of polar craters. Both of these lines of evidence are strengthened by the new Arecibo data.

The new results confirm earlier evidence for extreme brightness ( $\hat{\sigma} \sim 1$ ) and polarization inversion ( $\mu_c > 1$ ) of the polar echoes. It seems likely that the same basic scattering mechanism is responsible for such anomalous backscatter from the icy Galilean satellites and the martian and mercurian poles. Various mechanisms have been proposed to explain the Galilean satellite echoes, nearly all of which involve some form of subsurface or volume scattering. Among the more plausible of these is the so-called "coherent backscatter" effect, which combines multiple scattering off subsurface inhomogeneities with a coherence effect that boosts the strength and helicity retention of the backscattered wave (Hapke 1990, Peters 1992). This and similar theories require that the scattering occur within some low-loss matrix material than can support long subsurface path lengths with minimal attenuation. One such suitable medium would be a thick deposit of clean water ice containing internal scatterers such as cracks and voids. There is evidence for water ice being the predominant constituent of the surfaces of the icy Galilean satellites (Calvin *et al.* 1995). Water ice is also thought to make up Mars' north polar cap (Thomas *et al.* 2000), which

has recently been found to give enhanced radar backscatter at both S and X bands (Harmon *et al.* 1999, Butler *et al.* Radar reflectivity of the martian polar regions. 2nd Intl. Martian Polar Conf., Reykjavik, Iceland. 2000). Another potential scattering medium is CO<sub>2</sub> ice, which is considered by some to be the most likely constituent of Mars' residual south polar cap (Thomas *et al.* 2000) and thus a possible source of the radar feature from that pole. However, CO<sub>2</sub> ice is much less stable than H<sub>2</sub>O ice for a given temperature and thus an unlikely candidate for the Mercury volatiles. (Hence, for the remainder of this paper we will use the term "ice" as being synonymous with water ice.) An alternative material that has been seriously considered for Mercury's polar deposits is elemental sulfur (Sprague *et al.* 1995), a volatile which is more stable than water ice and which has the requisite low electrical conductivity.

Maintaining ice deposits on Mercury requires permanent shading from direct sunlight, which makes crater floors the most likely sites for such deposits. We have found that nearly all of the bright features on the photographed side (including the new features found in the 1998–1999 images) can be identified with craters, while the remainder are associated with other shaded areas. Also, many of the features on the unphotographed side show some distinctive crater morphology, such as circularity, radar shadowing/highlighting, or pole-facing symmetry. The locations, shapes, and extents of bright crater features on both the photographed and unphotographed sides suggest confinement to permanently shaded areas, as evidenced by the transition in feature shapes from circles to crescents to points or slivers as one goes from the pole to lower latitudes. This may explain the apparent affinity of radar features for c<sub>4</sub>-class craters, as evidenced by the fact that all 11 of the c<sub>4</sub>-class craters above 79° N show features, whereas only 1 or 2 of the 8 c<sub>3</sub>-class craters above 79° N do. Presumably, the longer shadows cast by the undegraded rims of the fresher craters result in a greater amount of permanent shading.

### 6.1. Comparisons with Thermal Models

**6.1.1. Preliminary models.** Rigorous thermal modeling shows that permanent shading from direct sunlight is not a sufficient condition for ensuring the low temperatures required to maintain surface water ice for billions of years (Paige *et al.* 1992). The reason is that one must also allow for the significant heating associated with indirect radiation, that is, scattered sunlight and infrared reradiation from the adjacent sunlit portions of crater floors and interior rim walls. This heating is stronger for low-latitude craters and for small craters with high depth/diameter ratios. Some preliminary modeling that includes these effects was done by Paige *et al.* (1992) and Ingersoll *et al.* (1992) soon after the discovery of the polar features. These models assumed for analytic simplicity that craters have hemispherical floors. Both studies showed that a typical undegraded crater of medium size cannot support ice at latitudes below 84°, based on calculated floor temperatures in excess of 112 K (the temperature at which sublimation would erode an ice deposit at

the rate of 1 m/Gyr). Citing these results, Harmon *et al.* (1994) pointed out the potential thermal problems for ice after identifying crater features (e.g., S and T) at latitudes below 80°. The sulfur hypothesis of Sprague *et al.* (1995) was offered, in part, as a response to these apparent problems.

**6.1.2. Modified models and thermal insulation.** In a recent finite-element analysis, Vasavada, Paige, and Wood (1999) (henceforth abbreviated VPW) refined the thermal modeling to include flat floors (more precisely, truncated cones) for medium to large size craters, retaining hemispherical floors only for those small, bowl-shaped craters for which this is still a reasonable approximation. Although their results showed that the coldest parts of flat-floored craters could have  $T < 112$  K at latitudes down to 82°, they found that the diurnal maximum surface temperatures were too high to support exposed water ice deposits in craters such as S, T, and W. Moreover, their analysis of some higher latitude craters (e.g., crater M) predicts the areal extent of exposed cold ( $T < 112$  K) surfaces to be smaller than the corresponding radar features in our new images. Only near-polar features such as D and E come close to being consistent with the VPW model for exposed water ice (compare our Fig. 3a with their Fig. 10).

VPW argue that one can reduce the diurnal range of crater floor temperatures by covering the ice with a thin insulating layer of dust. Adding a 0.1- to 0.5-m thick mantle would significantly increase the fraction of crater floor capable of harboring ice and at the same time protect any ice surface from sputtering and UV erosion. Inspection of the VPW thermal models for craters such as M and W shows that thermally insulated water ice deposits are consistent with the sizes and locations of the radar features within these craters (compare their Fig. 10 with our Fig. 3a). In fact, their crater models suggest that thermally protected ice deposits could account for the radar features from all of the original host craters identified by Harmon *et al.* (1994) in the photographed hemisphere (i.e., craters C, D, E, L, M, N, P, Q, R, S, T, W, and Y).

**6.1.3. Low-latitude craters.** The first test of the plausibility of ice explaining the lower latitude features is whether they satisfy the necessary condition of permanent shading from direct sunlight. For truncated-cone craters, the limiting latitude  $\phi_{\min}$  for permanent shading is simply given by  $\phi_{\min} = 90^\circ - s$ , where  $s$  is the slope of the interior rim wall. Using some relations from Pike (1988) we get  $\phi_{\min} = 76.5\text{--}78.2^\circ$  for crater diameters in the range 30–150 km, dropping to  $\phi_{\min} \leq 70^\circ$  for craters with diameters of 20 km or less. These results are in good agreement with the latitude limits shown in Fig. 13 of VPW. It seems plausible, then, that one could have small areas of permanent shade surviving under the south walls of some of the steeper-walled craters down to the 72° latitude limit of our observed radar features. Small-scale topography on the lower rim walls might also provide some extra shading for some low-latitude craters. These arguments are consistent with the fact that all of our low-latitude features are either small points or narrow slivers with their long axes perpendicular to the pole direction. Therefore, we do not

think that one can discount the existence of water ice in any of our low-latitude features strictly on the basis of a lack of permanent shading.

A greater problem for maintenance of water ice at low latitudes is with indirect heating, which becomes stronger with lower latitude. The problem largely goes away (for medium to large craters with permanent shading) if one invokes a protective mantle, since such insulation substantially reduces both temperature and the latitude dependence of temperature (see Fig. 12b of VPW). But then one is still left with the problem of accumulating a mantle quickly enough to prevent complete erosion of any initially exposed ice deposit (see Section 6.2), which does become more difficult at lower latitudes (see Fig. 12a of VPW). A case in point is crater W (Despréz), in which diurnal maximum surface temperatures should exceed 140 K everywhere except for a tiny region much smaller than the size of the radar feature (see Fig. 10 of VPW). The problem is still worse for craters S and T, for which VPW predict diurnal maximum surface temperatures of 150 K in the coldest parts of the floors. Although S and T are only slightly lower in latitude than W, they should suffer stronger indirect heating owing to their hot longitudes and smaller diameters. For yet smaller craters the thermal problems become severe at all latitudes, as is discussed next.

**6.1.4. Small craters.** Both Paige *et al.* (1992) and VPW showed that no permanent ice should be expected in the exposed floors of small (diameter <10 km) craters at any latitude. This is because the floors of these craters, which are approximately isothermal, receive high levels of indirect radiation owing to their bowl shapes and high depth/diameter ratios. VPW also showed that mantling, while significantly lowering floor temperatures, only lowers the latitude limit for ice in small craters to 88°. Our new images therefore pose a problem for the water-ice hypothesis, since they reveal bright features in several small (<10 km) craters on the photographed side (all but one of which are at latitudes below 88°) as well as a number of small or unresolved features on the unphotographed side that may also come from small craters.

A possible way around this problem would be if those small craters containing radar features happened, for some reason, to be shallower than typical fresh craters of their size. Such might be the case if they were secondary craters produced at low impact velocities or were blanketed by ejecta from later, nearby impacts. These conditions might hold for features such as A2, F2, and H2, which are adjacent to larger craters and also close enough (lat. >87°N) to the pole to receive relatively little sunlight. It would be hard to make the same case for features R2, S2, T2, and W2, which are located in isolated craters and at lower latitudes (≤86°N). Inspection of the Mariner-10 images shows many small craters lacking radar features, so it may simply be that the small, radar-bright craters represent the shallow end of the depth distribution. These caveats notwithstanding, the existence of small, radar-bright craters should be considered a potential problem for the water-ice hypothesis and a topic to be addressed by future theoretical work.

**6.1.5. Polar caps and the “diffuse patch.”** Paige *et al.* (1992) and VPW showed that one should not see true “ice caps” (i.e., continuous expanses of water ice in flat, unshaded terrain), either exposed or mantled, on Mercury. Barlow *et al.* (1999) found no evidence for terrain-softening indicative of a primordial ice cap, although their study was necessarily restricted to craters below 85°N latitude. Butler (1997) states that sulfur, a more stable volatile than water ice, could form permanent polar caps above 88° latitude, while VPW give 86° as the latitude limit for a buried sulfur cap. The closest thing to a polar cap that we see in our images is the diffuse patch. However, this feature is not symmetric about the pole, but rather is concentrated around craters E, H, J, and K. Therefore, while we cannot rule out a buried sulfur cap, we think it more likely that the diffuse patch is not a true polar cap but rather a dense collection of small volatile deposits concentrated in shallow depressions and secondaries within the hummocky ejecta blankets of these craters. The faintness of the diffuse patch may then be just a filling-factor effect, with the radar-bright deposits concentrated only in suitable depressions rather than constituting continuous sheets.

## 6.2. Deposition Processes and Time Scales

The foregoing discussion naturally invites consideration of possible scenarios for the deposition of polar ice and of any insulating mantle that may be required by thermal models.

We are very limited in what we can infer about depositional processes and chronologies from the radar data itself. The association of bright features with  $c_4$ -class craters indicates that most of the observed volatiles were deposited after the Caloris event and well after the start of smooth plains emplacement. Furthermore, the discovery of radar features in craters P, Q, Despréz, Tung Yuan, and others shows that at least some of the volatiles were deposited after the emplacement of smooth plains in Goethe basin and northern Borealis Planitia. Barlow *et al.* (1999) propose that the lack of radar features in the fresher  $c_5$ -class craters suggests that no ice was deposited after the Mansurian period (3.0–3.5 Gyr ago). However, the north polar geologic map of Grolier and Boyce (1984) does not include a  $c_5$  class. Also, the south polar geologic map of Strom *et al.* (1990) does not show any  $c_5$ -class craters within 11° of the south pole, and the Arecibo radar map of that pole (Harmon *et al.* 1994, Harmon 1997) was too noisy to check for weak, low-latitude features. Therefore, we do not think there is justification for setting a lower limit for the age of the polar volatiles based on the existing data.

The possible sources of polar ice include *endogenic* release of water vapor through volcanism or other outgassing and *exogenic* delivery through impacts (of comets, asteroids, and meteors) or solar wind implantation (which reduces surface iron). Endogenic scenarios are not only very uncertain, as was pointed out by Arnold (1979) in the lunar-ice context, but also face some obvious problems in the case of Mercury. No volcanoes were found in the Mariner-10 images, and much if not most of the smooth plains effusion (and any associated release of water vapor) must have pre-dated the formation of the radar-bright  $c_4$  craters. Also,

these craters were apparently formed during a late stage of the planet's early senescence, by which time planetary cooling and contraction should have choked off most incipient volcanism. It is possible, of course, that volcanic constructs will eventually be found in the unphotographed hemisphere; in fact, Harmon (1997) suggested that one of the prominent mid-latitude radar features in this hemisphere might be a large volcano, although this remains speculative and an impact origin is also possible. Robinson and Lucey (1997) found evidence for possible pyroclastic volcanism from Mariner-10 color image data, but it is not clear how recent or widespread such volcanism might have been.

Exogenic delivery scenarios are more amenable to quantitative analysis, and perhaps more plausible, than endogenic ones. Both Killen *et al.* (1997) and Moses *et al.* (1999) have argued that exogenic sources could have delivered as much as meters or even tens of meters of water to polar cold traps over the past few billion years, with short-period, Jupiter-family comets being the most important contributors. The highest deposition rate entertained by Moses *et al.* (1999) is 20 m/Gyr. This would just match the erosion rate from sublimation at a temperature of 118 K, which corresponds to the coldest exposed, permanently shaded surface in a 40-km-diameter crater at 80° latitude and a hot longitude (see VPW). The work of VPW suggests that indirect heating is about 25% less at cold longitudes, which might lower the corresponding latitude limit to 70° at these longitudes. It is therefore just possible that, even without mantling, there is some net accumulation of ice in the very coldest portions of many of our radar-bright craters, including those below 75° latitude. However, as was pointed out in Section 6.1.3, one would not expect there to be any ice accumulation at all in some craters such as S and T, nor could accumulations of exposed ice explain the sizes of many features such as W. Invoking protective mantling to solve the problem does not help if the ice deposition is continuous, since new ice would still sublime as soon as it was emplaced. Mantling might facilitate an ice buildup if the delivery of ice is highly episodic, with thick deposits laid down in one or more major impacts followed by accumulation of an insulating cover on a time scale shorter than the evaporative erosion time for each deposit. Killen *et al.* (1997) estimate that it takes roughly a half-billion years to accumulate a decimeter-thick soil mantle from local impacts and mass wasting, by which time at least 10 m of ice would have evaporated from a deposit in a 40-km crater at 80° latitude and a hot longitude (assuming the VPW sublimation rate). A higher dust deposition rate, such as the 2 m/Gyr rate proposed for the Moon by Gault *et al.* (1974), could lower this ice erosion to more acceptable values, but would also result in strong attenuation of the radar wave in the overlying mantle. For example, a 2-m-thick mantle with the electrical properties of the typical mercurian surface (Mitchell and de Pater 1994) would attenuate the ice echo by 80% at S-band and even more at X-band. An appealing alternative is the suggestion by VPW that a thick deposit of dirty ice could form its own self-sealing mantle from the residue left over from surface evaporation. However, this begs the question of how one could get dirt mixed in with rapidly emplaced, cold-trapped ice in the first

place. Mixing dirt with volatiles as part of the impact process is problematic, since the characteristic time scale of 12 h given by Butler (1997) for the migration and cold-trapping of water molecules is much longer than the ~20-min ballistic settling time for any planet-wide blanket of ejecta from the same impact (as estimated from the time required to traverse one planet radius at half the escape velocity).

## 7. DISCUSSION AND CONCLUSION

There should be little doubt at this point that polar craters on Mercury contain cold-trapped volatiles. Since the enhanced radar backscatter is almost surely a volume scattering process, the deposits must be relatively thick and clean, and composed of a volatile substance with low electrical conductivity. There remain very compelling reasons for supposing that the volatile in question is water ice. First, it is believed to be responsible for the anomalous backscatter from the Galilean satellites and one (or possibly both) of the martian ice caps. Second, it is the most abundant volatile in the Solar System and the most likely candidate for exogenic delivery via comets or asteroids (Moses *et al.* 1999). However, there are potentially serious thermal problems with water ice, as was pointed out in the previous section. While it appears that a thermally insulating mantle could protect the ice in many of the observed features, burying it on a sufficiently short time scale may be a problem, especially at the lower latitudes where floor temperatures are higher and the erosion rate for exposed ice is correspondingly higher. It may also be hard to explain some of the radar features coming from very small craters.

Clearly, more theoretical work should be done to address the various issues and problems surrounding the water-ice hypothesis. In particular, consideration should be given to any other effects that could either lower the average temperatures within craters or lower the net rate of ice loss at a given temperature. VPW left open the possibility that their sublimation rate extrapolations to low temperatures may actually overestimate the sublimation, which is not inconceivable given the extreme sensitivity of sublimation rate to small temperature changes. In fact, both Butler *et al.* (1993) and Killen *et al.* (1997) adopt sublimation rates that are actually higher than those used by VPW. However, calculations by Killen *et al.* (1997) also suggest that the net loss rate for water ice deposits can be drastically lowered by including the diffusion-barrier effects of even a thin (1–2 cm) dust mantle or by requiring that any permanent water loss include at least photodissociation and possibly also ionization. Also worth considering are the potential thermal effects of complex crater floor geometries and structures. The recent work of Carruba and Coradini (1999) on the “double-shielding” effect for embedded craters is an example of this, and small-scale topography in crater floors may also provide some extra shielding from indirect radiation. Other possibilities are that exogenic water delivery rates are (or were in the past) much higher than estimated in recent studies and that the ice we now see on Mercury is from a very recent impact. Finally, work should continue on alternative volatiles, along the same lines as the sulfur

proposal of Sprague *et al.* (1995), as well as on the possibility that more than one volatile species is involved.

The answers to some of the outstanding questions may have to await new observations. The most critical need is for new spectrographic results aimed at determining the volatile species. Atmospheric OH from fresh polar ice would be observable with ground-based or Earth-orbiting UV spectrometry, but buried deposits would be difficult to detect (Killen *et al.* 1997). It seems likely, then, that spectrometric confirmation of water ice will require a spacecraft mission. A neutron spectrometer such as that planned for the Messenger orbiter would be capable of detecting buried or exposed H<sub>2</sub>O hydrogen in polar deposits and of distinguishing water ice from sulfur (Feldman *et al.* 1997). An orbiting UV spectrometer could also be used to search for buried ice deposits (Killen *et al.* 1997) or sulfur deposits emitting the 1814 Å line (Sprague *et al.* 1995). In the mean time, observations will continue using Earth-based radars. Goldstone X-band images, such as those recently obtained by Slade *et al.* (2000) with the long-code method, can be compared with Arecibo S-band images to check for attenuation in any overlying dust mantle; for example, attenuation in a 20-cm-thick mantle can be expected to reduce the X-band echo power to 65% of the S-band power. Arecibo observations are also planned to improve the north polar resolution still further as well as to obtain comparable high-quality images of the south pole when it returns to our view after 2003.

Finally, insight into the Mercury ice question may come out of the recent and ongoing search for lunar ice. The neutron spectrometer on the Lunar Prospector orbiter detected hydrogen concentrations at the lunar poles that may indicate water ice deposits (Feldman *et al.* 1998). Feldman *et al.* (2000) report that the strongest hydrogen signature at the lunar south pole comes from Shoemaker Crater, whose entire floor is known to be permanently shaded based on radar interferometry (Margot *et al.* 1999). This provides some support, if only indirect, for the plausibility of cold-trapped water ice concentrating at Mercury's poles. However, the absence of enhanced radar backscatter features from the lunar poles (Stacy *et al.* 1997, Simpson and Tyler 1999) argues that any lunar ice is likely to be in the form of a dilute frost mixed into the regolith rather than the thick deposits of relatively clean ice that are required to explain the Mercury echoes; Feldman *et al.* (2000) estimate the concentration by weight of the putative lunar ice to be only 1.5% based on a comparison of the neutron spectrometer data with radar topographic estimates of crater shading. Harmon (1997) argued that if ice were found on Mercury but not on the Moon, then exogenic sources for the Mercury ice would appear unlikely and differences in the crustal chemistry and/or outgassing histories of the two bodies would be implied. The same argument might be offered to explain any large differences in the amounts of ice at the poles of the two bodies. An alternative way to explain the difference would be if Mercury and the Moon had very different obliquity histories; Mercury's spin vector probably settled quickly into its current state (Peale 1974), whereas the Moon's may have evolved more slowly from an initially high obliquity

(Ward 1975). This would favor Mercury over the Moon as an ice habitat in any scenarios in which most of the water is supplied early in Solar System history. Finally, the relative amounts of ice on these two bodies could simply be a matter of chance, especially if one favors exogenic delivery scenarios dominated by one or more massive impacts.

## ACKNOWLEDGMENTS

We are grateful to Tony Crespo and Mike Nolan for their assistance during the observations. We also recognize the crucial role played by Don Campbell in the upgrading of the telescope and in the planning and development of the new S-band radar. People with whom we had fruitful discussions or who offered helpful comments on the manuscript include R. Killen, D. Campbell, J.-L. Margot, W. Feldman, B. Butler, and A. Vasavada. The National Astronomy and Ionosphere Center (Arecibo Observatory) is operated by Cornell University under a cooperative agreement with the National Science Foundation and with support from the National Aeronautics and Space Administration.

## REFERENCES

- Arnold, J. R. 1979. Ice in the lunar polar regions. *J. Geophys. Res.* **84**, 5659–5668.
- Barlow, N. G., R. A. Allen, and F. Vilas 1999. Mercurian impact craters: Implications for polar ground ice. *Icarus* **141**, 194–204.
- Butler, B. J. 1994. *3.5-cm radar investigation of Mars and Mercury: Planetary implications*. Ph.D. thesis, Calif. Inst. of Technol., Pasadena.
- Butler, B. J. 1997. The migration of volatiles on the surfaces of Mercury and the Moon. *J. Geophys. Res.* **102**, 19,283–19,291.
- Butler, B. J., D. O. Muhleman, and M. A. Slade 1993. Mercury: Full-disk radar images and the detection and stability of ice at the north pole. *J. Geophys. Res.* **98**, 15,003–15,023.
- Calvin, W. M., R. N. Clark, R. H. Brown, and J. R. Spencer 1995. Spectra of the icy Galilean satellites from 0.2 to 5  $\mu\text{m}$ : A compilation, new observations, and a recent summary. *J. Geophys. Res.* **100**, 19,041–19,048.
- Campbell, D. B., J. F. Chandler, S. J. Ostro, G. H. Pettengill, and I. I. Shapiro 1978. Galilean satellites: 1976 radar results. *Icarus* **34**, 254–267.
- Carruba, V., and A. Coradini 1999. Lunar cold traps: Effects of double shielding. *Icarus* **142**, 402–413.
- Davies, M. E., T. R. Colvin, M. S. Robinson, and K. Edwards 1996. Mercury's polar regions: Locations of radar anomalies (ice). *Bull. Am. Astron. Soc.* **28**, 1115.
- Davies, M. E., S. E. Dwornik, D. E. Gault, and R. G. Strom 1978. *Atlas of Mercury*. NASA, Washington, DC.
- Feldman, W. C., B. L. Barraclough, C. J. Hansen, and A. L. Sprague 1997. The neutron signature of Mercury's volatile polar deposits. *J. Geophys. Res.* **102**, 25,565–25,574.
- Feldman, W. C., D. J. Lawrence, R. C. Elphic, B. L. Barraclough, S. Maurice, I. Genetay, and A. B. Binder 2000. Polar hydrogen deposits on the Moon. *J. Geophys. Res.* **105**, 4175–4195.
- Feldman, W. C., S. Maurice, A. B. Binder, B. L. Barraclough, R. C. Elphic, and D. J. Lawrence 1998. Fluxes of fast and epithermal neutrons from Lunar Prospector: Evidence for water ice at the lunar poles. *Science* **281**, 1496–1500.
- Gault, D. E., F. Hörz, D. E. Brownlee, and J. B. Hartung 1974. Mixing of the lunar regolith. *Proc. Lunar. Planet. Sci. Conf. 5th*, 2365–2386.
- Grolier, M. J., and J. M. Boyce 1984. Geologic map of the Borealis region of Mercury. USGS Map I-1660, U.S. Geol. Surv., Reston, VA.
- Hapke, B. 1990. Coherent backscatter and the radar characteristics of the outer planet satellites. *Icarus* **88**, 407–417.
- Harmon, J. K. 1997. Mercury radar studies and lunar comparisons. *Adv. Space Res.* **19**(10), 1487–1496.

- Harmon, J. K., and M. A. Slade 1992. Radar mapping of Mercury: Full-disk images and polar anomalies. *Science* **258**, 640–643.
- Harmon, J. K., D. B. Campbell, D. L. Bindschadler, J. W. Head, and I. I. Shapiro 1986. Radar altimetry of Mercury: A preliminary analysis. *J. Geophys. Res.* **91**, 385–401.
- Harmon, J. K., M. A. Slade, and R. S. Hudson 1992. Mars radar scattering: Arecibo/Goldstone results at 12.6- and 3.5-cm wavelengths. *Icarus* **98**, 240–253.
- Harmon, J. K., M. A. Slade, R. A. Vélez, A. Crespo, M. J. Dryer, and J. M. Johnson 1994. Radar mapping of Mercury's polar anomalies. *Nature* **369**, 213–215.
- Harmon, J. K., R. E. Arvidson, E. A. Guinness, B. A. Campbell, and M. A. Slade 1999. Mars mapping with delay-Doppler radar. *J. Geophys. Res.* **104**, 14,065–14,090.
- Ingersoll, A. P., T. Svittek, and B. C. Murray 1992. Stability of polar frosts in spherical bowl-shaped craters on the Moon, Mercury, and Mars. *Icarus* **100**, 40–47.
- Killen, R. M., J. Benkhoff, and T. H. Morgan 1997. Mercury's polar caps and the generation of an OH exosphere. *Icarus* **125**, 195–211.
- Kumar, S. 1976. Mercury's atmosphere: A perspective after Mariner 10. *Icarus* **28**, 579–591.
- Margot, J.-L., D. B. Campbell, R. F. Jurgens, and M. A. Slade 1999. Topography of the lunar poles from radar interferometry: A survey of cold trap locations. *Science* **284**, 1658–1660.
- Mitchell, D. L., and I. de Pater 1994. Microwave imaging of Mercury's thermal emission at wavelengths from 0.3 to 20.5 cm. *Icarus* **110**, 2–32.
- Moses, J. I., K. Rawlins, K. Zahnle, and L. Dones 1999. External sources of water for Mercury's putative ice deposits. *Icarus* **137**, 197–221.
- Muhleman, D. O., B. J. Butler, A. W. Grossman, and M. A. Slade 1991. Radar images of Mars. *Science* **253**, 1508–1513.
- Ostro, S. J., and 11 colleagues 1992. Europa, Ganymede, and Callisto: New radar results from Arecibo and Goldstone. *J. Geophys. Res.* **97**, 18,227–18,244.
- Paige, D. A., S. E. Wood, and A. R. Vasavada 1992. The thermal stability of water ice at the poles of Mercury. *Science* **258**, 643–646.
- Peale, S. J. 1974. Possible histories of the obliquity of Mercury. *Astron. J.* **79**, 722–744.
- Peters, K. J. 1992. Coherent-backscatter effect: A vector formalism accounting for polarization and absorption effects and small or large scatterers. *Phys. Rev. B* **46**, 801–812.
- Pike, R. J. 1988. Impact craters on Mercury. In *Mercury* (F. Vilas, C. R. Chapman, and M. S. Matthews, Eds.), pp. 165–273. Univ. of Arizona Press, Tucson.
- Robinson, M. S., and P. G. Lucey 1997. Recalibrated Mariner 10 color mosaics: Implications for mercurian volcanism. *Science* **275**, 197–200.
- Robinson, M. S., M. E. Davies, T. R. Colvin, and K. E. Edwards 1999. A revised control network for Mercury. *J. Geophys. Res.* **104**, 30,847–30,852.
- Salvail, J. R., and F. P. Fanale 1994. Near-surface ice on Mercury and the Moon: A topographic thermal model. *Icarus* **111**, 441–455.
- Simpson, R. A., and G. L. Tyler 1999. Reanalysis of Clementine bistatic radar data from the lunar south pole. *J. Geophys. Res.* **104**, 3845–3862.
- Slade, M. A., B. J. Butler, and D. O. Muhleman 1992. Mercury radar imaging: Evidence for polar ice. *Science* **258**, 635–640.
- Slade, M. A., L. J. Harcke, R. F. Jurgens, J. K. Harmon, H. A. Zebker, and E. M. Standish 2000. 3.5-cm imaging of the Mercury north polar radar bright features (abstract). Lunar Planet. Sci. Conf. 31st, Houston, Texas.
- Sprague, A. L., D. M. Hunten, and K. Lodders 1995. Sulfur at Mercury, elemental at the poles and sulfides in the regolith. *Icarus* **118**, 211–215.
- Stacy, N. J. S., D. B. Campbell, and P. G. Ford 1997. Arecibo radar mapping of the lunar poles: A search for ice deposits. *Science* **276**, 1527–1530.
- Strom, R. G., M. C. Malin, and M. A. Leake 1990. Geologic map of the Bach region of Mercury. USGS Map I-2015, U.S. Geol. Surv., Reston, VA.
- Thomas, G. E. 1974. Mercury: Does its atmosphere contain water? *Science* **183**, 1197–1198.
- Thomas, P. C., M. C. Malin, K. S. Edgett, M. H. Carr, W. K. Hartmann, A. P. Ingersoll, P. B. James, L. A. Soderblom, J. Veverka, and R. Sullivan 2000. North–south geological differences between the residual polar caps on Mars. *Nature* **404**, 161–164.
- Vasavada, A. R., D. A. Paige, and S. E. Wood 1999. Near-surface temperatures on Mercury and the Moon and the stability of polar ice deposits. *Icarus* **141**, 179–193.
- Ward, W. 1975. Past orientation of the lunar spin axis. *Science* **189**, 377–379.
- Watson, K., B. C. Murray, and H. Brown 1961. The behavior of volatiles on the lunar surface. *J. Geophys. Res.* **66**, 3033–3045.